

The inverse cascade and nonlinear alpha-effect in simulations of isotropic helical hydromagnetic turbulence

Axel Brandenburg^{1,2}

Institute for Theoretical Physics, Kohn Hall, University of California, Santa Barbara, CA 93106

`brandenb@nordita.dk` (May 20, 2019)

ABSTRACT

A numerical model of isotropic homogeneous turbulence with helical forcing is investigated. The resulting flow, which is essentially the prototype of the α^2 dynamo of mean-field dynamo theory, produces strong dynamo action with an additional large scale field on the scale of the box (at wavenumber $k = 1$; forcing is at $k = 5$). This large scale field is nearly force-free and exceeds the equipartition value. As the magnetic Reynolds number R_m increases, the saturation field strength and the growth rate of the dynamo increase. However, the time it takes to built up the large scale field from equipartition to its final super-equipartition value increases with magnetic Reynolds number. The large scale field generation can be identified as being due to nonlocal interactions originating from the forcing scale, which is characteristic of the α -effect. Both α and turbulent magnetic diffusivity are determined simultaneously using numerical experiments where the mean-field is modified artificially. Both quantities are quenched in a R_m -dependent fashion. Nevertheless, the final equilibrium strength of the large scale field *increases* weakly with R_m . The results are numerically robust in that the shape of the spectrum at large scales is unchanged when changing the resolution from 30^3 to 120^3 meshpoints, or when increasing the magnetic Prandtl number (viscosity/magnetic diffusivity) from 1 to 100. Increasing the forcing wavenumber to 30 (i.e. increasing the scale separation) makes the inverse cascade effect more pronounced, although it remains otherwise qualitatively unchanged.

Subject headings: MHD – turbulence

1. Introduction

The generation of large scale magnetic fields from small scale turbulence is important in many astrophysical bodies (planets, stars, accretion discs and galaxies). Over many decades the $\alpha - \omega$ dynamo concept has been invoked to explain large scale magnetic field generation (Moffatt 1978, Parker 1979, Krause & Rädler 1980). Over recent years however numerical simulations have become available that produce large scale fields with appreciable magnetic energy, sometimes even exceeding the turbulent kinetic energy (e.g. Glatz-

maier & Roberts 1995, Brandenburg *et al.* 1995, Ziegler & Rüdiger 2000). Whether or not large scale field generation to such amplitudes is related to the α -effect remains debatable (e.g. Cattaneo & Hughes 1996, Brandenburg & Donner 1997).

The purpose of this paper is to study a simple system that is prototypical of the α -effect: homogeneous isotropic turbulence that lacks mirror symmetry. This is accomplished by adopting a body force corresponding to plane polarized waves in random directions (but constant polarization) with wavelengths short compared with the size of the box. Since the seminal papers by Frisch *et al.* (1975) and Pouquet, Frisch, & Léorat (1976) we know that there should be an inverse cascade of magnetic helicity, which has also been demonstrated using direct numerical simu-

¹Permanent address: Nordita, Blegdamsvej 17, DK-2100 Copenhagen Ø, Denmark

²Also at: Department of Mathematics, University of Newcastle, Newcastle upon Tyne, NE1 7RU, UK

lations (e.g. Meneguzzi, Frisch, & Pouquet 1981, Balsara & Pouquet 1999). However, to our knowledge there has never been a detailed study of the spatial magnetic field patterns obtained from the inverse cascade, nor has there been a quantitative identification of the classical α -effect in mean-field dynamo theory. Furthermore, the Reynolds and Prandtl number dependences of this process have not been fully explored yet. In the present paper we study models with strongly helical forcing at different Reynolds numbers. We also investigate some models where the magnetic Prandtl number (viscosity/magnetic diffusivity) is increased from 1 to 100. This may be important in connection with the galactic magnetic field, and there are some serious concerns that the inverse cascade may not be efficient at large magnetic Reynolds numbers.

2. The model

We consider a compressible isothermal gas with constant sound speed c_s , constant dynamical viscosity μ , constant magnetic diffusivity η , and constant magnetic permeability μ_0 . The governing equations for density ρ , velocity \mathbf{u} , and magnetic vector potential \mathbf{A} , are given by

$$\frac{D \ln \rho}{D t} = -\nabla \cdot \mathbf{u}, \quad (1)$$

$$\frac{D \mathbf{u}}{D t} = -c_s^2 \nabla \ln \rho + \frac{\mathbf{J} \times \mathbf{B}}{\rho} + \frac{\mu}{\rho} (\nabla^2 \mathbf{u} + \frac{1}{3} \nabla \nabla \cdot \mathbf{u}) + \mathbf{f}, \quad (2)$$

$$\frac{\partial \mathbf{A}}{\partial t} = \mathbf{u} \times \mathbf{B} - \eta \mu_0 \mathbf{J}, \quad (3)$$

where $D/Dt = \partial/\partial t + \mathbf{u} \cdot \nabla$ is the advective derivative, $\mathbf{B} = \nabla \times \mathbf{A}$ is the magnetic field, $\mathbf{J} = \nabla \times \mathbf{B}/\mu_0$ is the current density, and \mathbf{f} is a random forcing function.

We use periodic boundary conditions in all three directions for all variables. This implies that the mass in the box is conserved, i.e. $\langle \rho \rangle = \rho_0$, where ρ_0 is the value of the initially uniform density, and angular brackets denote volume averages. We adopt a forcing function \mathbf{f} of the form

$$\mathbf{f}(\mathbf{x}, t) = N \mathbf{f}_{\mathbf{k}(t)} \exp[i\mathbf{k}(t) \cdot \mathbf{x} + i\phi(t)] + \text{c.c.}, \quad (4)$$

where $\mathbf{k}(t) = (k_x, k_y, k_z)$ is a time dependent wavevector, $\mathbf{x} = (x, y, z)$ is position, and $\phi(t)$ with $|\phi| < \pi$ is a random phase. On dimensional grounds the normalization factor is chosen to be

$N = f_0 c_s (k c_s / \delta t)^{1/2}$, where f_0 is a nondimensional factor, $k = |\mathbf{k}|$, and δt is the length of the timestep. We focus on the case where $|\mathbf{k}|$ is around 5, and select at each timestep randomly one of the 228 possible vectors in $4.5 < |\mathbf{k}| < 5.5$. We force the system with eigenfunctions of the curl operator,

$$\mathbf{f}_{\mathbf{k}} = \frac{i\mathbf{k} \times (\mathbf{k} \times \hat{\mathbf{e}}) + |\mathbf{k}|(\mathbf{k} \times \hat{\mathbf{e}})}{2k^2 \sqrt{1 - (\mathbf{k} \cdot \hat{\mathbf{e}})^2/k^2}}, \quad (5)$$

where $\hat{\mathbf{e}}$ is an arbitrary unit vector needed in order to generate a vector $\mathbf{k} \times \hat{\mathbf{e}}$ that is perpendicular to \mathbf{k} . Note that $|\mathbf{f}_{\mathbf{k}}|^2 = 1$ and, in particular, $i\mathbf{k} \times \mathbf{f}_{\mathbf{k}} = |\mathbf{k}| \mathbf{f}_{\mathbf{k}}$, so the helicity density of this forcing function satisfies

$$\mathbf{f} \cdot \nabla \times \mathbf{f} = |\mathbf{k}| \mathbf{f}^2 > 0 \quad (6)$$

at each point in space. We note that since the forcing function is like a delta-function in \mathbf{k} -space, this means that all points of \mathbf{f} are correlated at any instant in time, but are different at the next timestep. Thus, the forcing function is delta-correlated in time (but the velocity is not).

We adopt nondimensional quantities by measuring \mathbf{u} in units of c_s , \mathbf{x} in units of $1/k_1$, where k_1 is the smallest wave number in the box, which has a size of $L = 2\pi$, density in units of ρ_0 , and \mathbf{B} is measured in units of $\sqrt{\mu_0 \rho_0} c_s$. This is equivalent to putting

$$c_s = k_1 = \rho_0 = \mu_0 = 1. \quad (7)$$

In the following we always quote the *mean* kinematic viscosity $\nu \equiv \mu/\rho_0$, which is close to the actual kinematic viscosity μ/ρ because the Mach numbers considered in the present paper are less than one.

We advance the equations in time using a third order Runge-Kutta scheme and sixth order explicit centered derivatives in space. In all cases presented we chose $f_0 = 0.1$, which yields rms Mach numbers around 0.1–0.3, and peak values less than one.

Our initial condition is $\ln \rho = \mathbf{u} = 0$, and \mathbf{A} is a smoothed gaussian random field that is delta-correlated in space, so the initial magnetic energy spectrum is $E_M(k) \sim k^4$ with a decline at high wavenumbers.

3. Results

In order to assess the Reynolds number dependence of our results we have performed three runs

with $\nu = \eta = 0.002$ (Run 1), $\nu = \eta = 0.005$ (Run 2), and $\nu = \eta = 0.01$ (Run 3); see Table 1 for a summary. In order to assess the dependence on magnetic Prandtl number we have two additional runs with $\nu = \eta = 0.02$ and $\nu/\eta = 20$ (Run 4) and 100 (Run 5). Those runs will be explained in detail in 3.5. In Runs 1–5 the forcing wavenumber was around 5, but in Run 6 we increased it to 30 in order to study the properties of larger scale separation; see 3.5. The root-mean-square values of various quantities are reasonably well converged, as can be gauged by comparing Run 2 (60^3 meshpoints) with Run 21 (30^3 meshpoints), which has the same values of η and ν . We return to a detailed discussion on the Reynolds number dependence in Sect 3.6.

In most of the plots below the approximate value of the magnetic Reynolds number (as given in the table) is used to identify the runs. We also give the Reynolds number based on the wavelength of the forcing, $R_{m,\text{forc}}$. The growth rate is determined as $\lambda = d \ln \langle \mathbf{B}^2 \rangle_{\text{lin}}^{1/2} / dt$, where the subscript ‘lin’ refers to early times when the field is still weak on all scales. A hyphen indicates that the run has been restarted from another run, so no data are available for the linear growth phase. Also given is the growth rate normalized with the turnover time $\tau = L / \langle \mathbf{u}^2 \rangle_{\text{lin}}^{1/2}$.

After about 30 time units the rms velocity, u_{rms} , reaches an approximate equilibrium amplitude of up to 0.3. (Since $c_s = 1$, this is also the Mach number.) This velocity corresponds to a turnover time of $L/u_{\text{rms}} \approx 20$ time units. The value of u_{rms} is somewhat smaller for smaller Reynolds number. The flow has strong positive helicity, as measured by the relative helicity $\langle \boldsymbol{\omega} \cdot \mathbf{u} \rangle / (u_{\text{rms}} u_{\text{rms}})$, which can be as large as 70% (or even larger when the Reynolds number is smaller). Here, $\boldsymbol{\omega} = \nabla \times \mathbf{u}$ is the vorticity.

The evolution of magnetic and kinetic energies (E_M and E_K) is shown in Fig. 1 for three values of the magnetic Reynolds number, $R_m = u_{\text{sat}} L / \eta$. Note that E_K decreases after E_M has reached its saturation value, so the values of R_m are based on the rms velocity during saturation, u_{sat} . The relative kinetic helicity changes only slightly before and after saturation. Both the growth rate and the saturation level of the magnetic field increase with increasing Reynolds number, and are likely

to reach some value independent of the Reynolds number at sufficiently large Reynolds number.

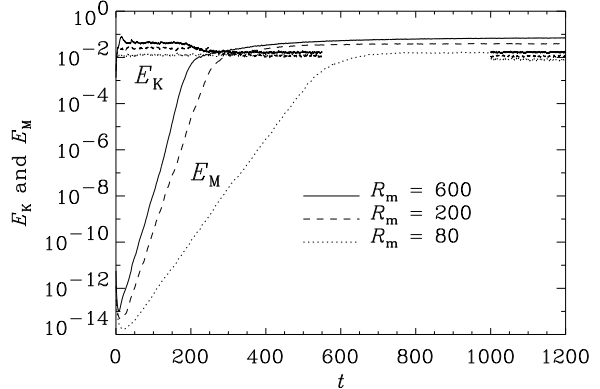


Fig. 1.— Evolution of magnetic energy and kinetic energy (per volume) for three values of the magnetic Reynolds number, R_m . Note that the growth rate and the saturation level increase with increasing R_m . For reasons of clarity the curves of kinetic energy are not shown in the range $550 < t < 1000$.

3.1. The inverse cascade

Consistent with previous studies in this field (e.g. Meneguzzi *et al.* 1981, Balsara & Pouquet 1999), we find the development of large scale fields through an inverse cascade effect of the magnetic helicity. This is best seen in the evolution of magnetic energy spectra, $E_M(k)$; see Fig. 2. The kinetic energy spectrum, $E_K(k)$, is also shown.

The random initial condition has a k^4 power-spectrum, corresponding to a delta-correlated vector potential. However, even though the initial field was smoothed, the spectrum is deformed significantly during the first few timesteps. During the interval $20 \leq t \leq 200$ the spectrum is nearly shape invariant and grows at all scales at the same rate; see Fig. 2. This is typical of small-scale dynamos (Kazantsev 1968).

At $t = 200$ the magnetic energy approaches equipartition with the kinetic energy at small scales. After $t = 240$ the magnetic energy is in slight superequipartition with the kinetic energy at $k > 10$. This marks the beginning of a more complicated process (Fig. 3) during which the field at the largest possible scale ($k = 1$)

TABLE 1
SUMMARY OF RUNS.

| | Run 1 | Run 2l | Run 2 | Run 3 | Run 3p | Run 4 | Run 5 | Run 6 |
|--|--------|--------|--------|---------|---------|---------|---------|---------|
| mesh points | 30^3 | 30^3 | 60^3 | 120^3 | 120^3 | 120^3 | 120^3 | 120^3 |
| ν | 0.01 | 0.005 | 0.005 | 0.002 | 0.002 | 0.02 | 0.02 | 0.002 |
| ν/η | 1 | 1 | 1 | 1 | 2 | 20 | 100 | 1 |
| k_{forcing} | 5 | 5 | 5 | 5 | 5 | 5 | 5 | 30 |
| $\langle \mathbf{u}^2 \rangle_{\text{lin}}^{1/2}$ | 0.16 | 0.23 | 0.22 | 0.29 | — | 0.11 | 0.114 | 0.082 |
| $\langle \mathbf{u}^2 \rangle_{\text{sat}}^{1/2}$ | 0.12 | 0.15 | 0.15 | 0.18 | 0.19 | 0.10 | 0.104 | 0.062 |
| R_m | 80 | 200 | 200 | 600 | 1200 | 700 | 3500 | 200 |
| R_m, forc | 16 | 40 | 40 | 120 | 240 | 140 | 700 | 8 |
| λ | 0.03 | 0.06 | 0.056 | 0.070 | — | 0.03 | 0.04 | 0.075 |
| $\lambda\tau$ | 1.2 | 1.6 | 1.7 | 1.5 | — | 1.7 | 2.4 | 5.7 |
| $\langle \mathbf{B}^2 \rangle_{\text{sat}}^{1/2}$ | 0.18 | 0.27 | 0.28 | 0.38 | 0.40 | > 0.2 | > 0.21 | > 0.2 |
| $\langle \mathbf{J}^2 \rangle_{\text{sat}}^{1/2}$ | 0.44 | 0.75 | 0.76 | 1.27 | 1.56 | 0.7 | 1.05 | 1.5 |
| $\langle \omega^2 \rangle_{\text{lin}}^{1/2}$ | 0.80 | 1.12 | 1.12 | 1.81 | — | 0.58 | 0.58 | 2.4 |
| $\langle \omega^2 \rangle_{\text{sat}}^{1/2}$ | 0.65 | 0.78 | 0.82 | 1.23 | 1.38 | 0.55 | 0.55 | 1.8 |
| $\langle \omega \cdot \mathbf{u} \rangle_{\text{lin}}$ | 0.13 | 0.24 | 0.24 | 0.37 | — | 0.063 | 0.063 | 0.20 |
| $\langle \omega \cdot \mathbf{u} \rangle_{\text{sat}}$ | 0.08 | 0.10 | 0.11 | 0.16 | 0.17 | 0.058 | 0.055 | 0.10 |
| $\langle \mathbf{J} \cdot \mathbf{B} \rangle_{\text{max}}$ | 0.007 | 0.025 | 0.027 | 0.07 | > 0.03 | 0.025 | > 0.06 | 0.040 |
| $\langle \mathbf{J} \cdot \mathbf{B} \rangle_{\text{max}} / (J_{\text{rms}} B_{\text{rms}})$ | 0.22 | 0.20 | 0.20 | 0.25 | — | 0.23 | 0.18 | 0.25 |
| $ \langle \mathbf{J} \cdot \mathbf{B} \rangle / \langle \mathbf{B}^2 \rangle _{\text{lin}}$ | 0.9 | 1.3 | 1.1 | 1-1.5 | — | 2.2 | 2.4 | 5.5 |

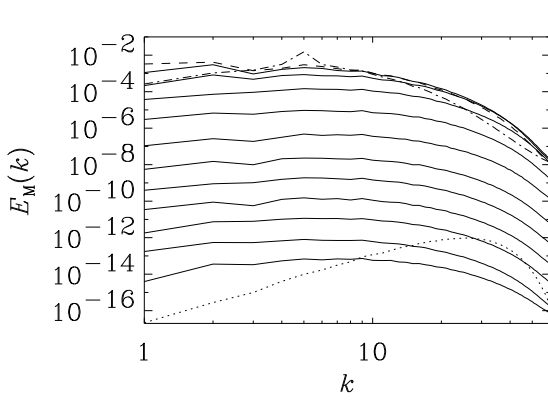


Fig. 2.— Spectra of magnetic energy for Run 3 during the initial growth phase at $t = 0$ (dotted line), $t = 20, 40, \dots, 220$ (solid lines) and $t = 240$ (dashed line). The kinetic energy spectrum (time averaged between $600 \leq t \leq 1000$) is shown for comparison (dash-dotted line give the kinetic energy spectrum).

continues to grow, but the field at intermediate wavenumbers ($k = 2, 3$, and 4) begins to decline. This process is essentially completed by the time $t = 400$. The significance of this process becomes clear when looking at the magnetic field evolution

in real space.

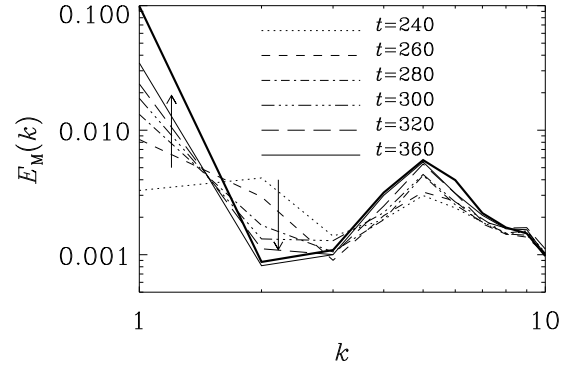


Fig. 3.— Spectra of magnetic energy for Run 3 during the saturation phase at times between $t = 240$ and 360 . The time averaged spectrum for times between 600 and 1000 is shown as a thick line. (Only the range $1 \leq k \leq 10$ is shown.)

3.2. The emergence of a large scale field

Although the magnetic field has reached equipartition already at $t \approx 200$, and its scale began to reach the largest possible scale of the box, it took another 100 time units for the large scale field

at scale $k = 1$ to fully develop and, more importantly, to suppress the power at intermediate scales. Looking at xy and yz cross-sections, two components of the field (B_x and B_z) show the development of a large scale sinusoidal modulation through the entire box. In Fig. 4 we show xy slices of B_x , but the yz cross-sections look qualitatively similar, except for a 90° phase shift of B_z in the y direction. This systematic phase shift is seen more clearly in a plot of the field averaged in the x and z directions; see Fig. 5.

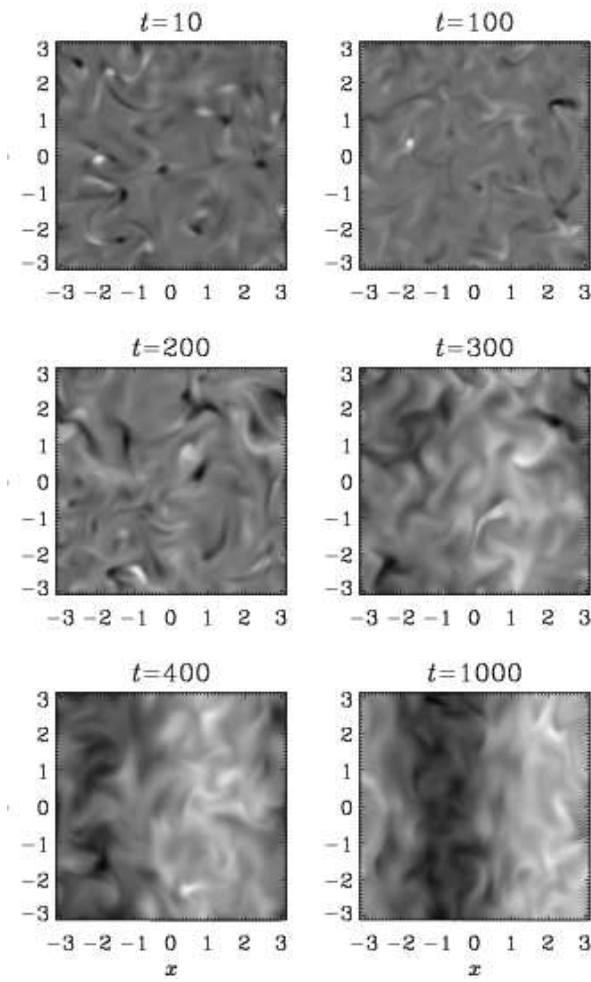


Fig. 4.— Gray-scale images of cross-sections of $B_x(x, y, 0)$ for Run 3 at different times showing the gradual build-up of the large scale magnetic field after $t = 300$. Dark (light) corresponds to negative (positive) values. Each image is scaled with respect to its min and max values.

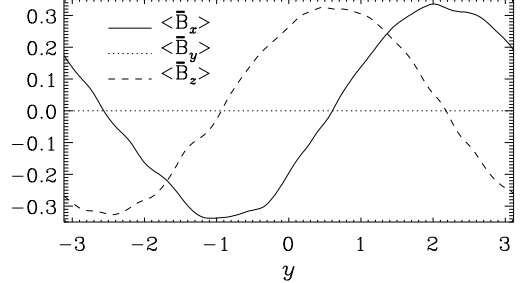


Fig. 5.— The three magnetic field components averaged in the x and z directions at $t = 1000$. Note the 90° phase shift between $\langle \bar{B}_x \rangle(y)$ and $\langle \bar{B}_z \rangle(y)$, and that the functional form is nearly sinusoidal. Run 3.

Although our forcing is isotropic, one particular direction has been selected by the large scale magnetic field. In Runs 1 and 3 it was the y -direction, in Run 2 the z -direction, and in Run 5 the x -direction. Which direction is selected depends on fine details of the initially random condition. Nevertheless, it is not until the time of saturation that the final selection is established, as can be seen in Fig. 6 where we plot the magnetic energies of the mean field for the three possible directions, denoted by $E(K_x)$, $E(K_y)$, $E(K_z)$. So,

$$E(K_x) = \langle \langle \mathbf{B} \rangle_{yz}^2 \rangle_x, \quad (8)$$

$$E(K_y) = \langle \langle \mathbf{B} \rangle_{xz}^2 \rangle_y, \quad (9)$$

$$E(K_z) = \langle \langle \mathbf{B} \rangle_{xy}^2 \rangle_z, \quad (10)$$

where the subscripts denote the directions of averaging. Those expressions mean that one first fixes a direction \mathbf{K} , say the x -direction, then defines mean fields by averaging in the two perpendicular directions, y and z , respectively, and then calculating the energy in this mean field. The time of selection, i.e. when the three $E(K_i)$ curves split, is somewhat earlier in the large Reynolds number cases.

The filling factor of the magnetic field may be measured by the ratio $\langle \mathbf{B} \rangle^2 / \langle \mathbf{B}^2 \rangle$, which characterizes the fraction of space occupied by the large scale field. Initially this ratio is just $\sim 2\%$ (for Run 3) and $\sim 0.7\%$ (for Run 5), but later it begins to level off near 80% (Fig. 7). Most likely real astrophysical dynamos are far less effective in

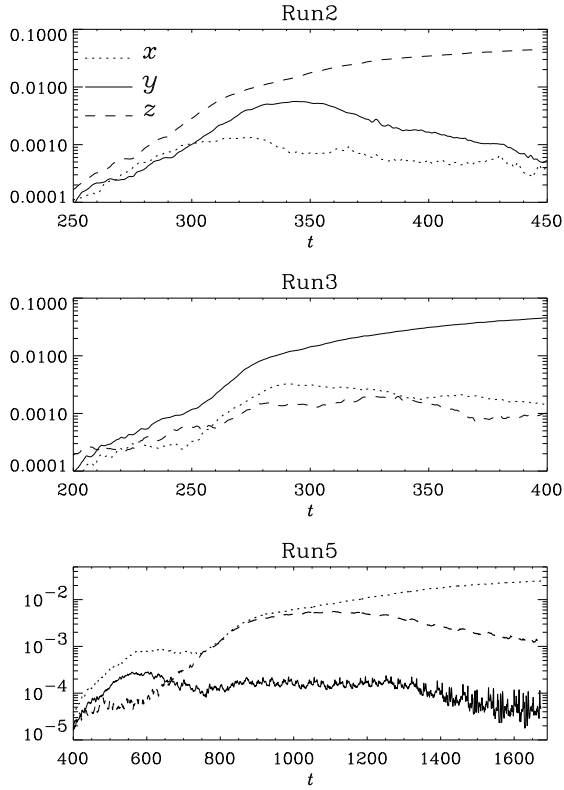


Fig. 6.— Magnetic energies (per volume) of the large scale field whose wave vectors point in the x , y , or z direction. Which of the three possible force-free solutions is selected in the end depends on chance.

producing such clean large scale fields, because in reality the helicity of the effective forcing will be far less than 100%. Nevertheless, it is important to notice that it is at least theoretically possible to achieve large scale field energies near or in excess of the kinetic energy, even though the magnetic Reynolds number is reasonably high.

We note that the phase of the large scale field may be drifting slowly as long as the large scale magnetic energy has not yet reached a fully steady state. In Run 3, for example, the phase was still drifting slowly in the y direction (speed $\sim +1.5\eta k_1$), but then it began to settle after $t \approx 1000$.

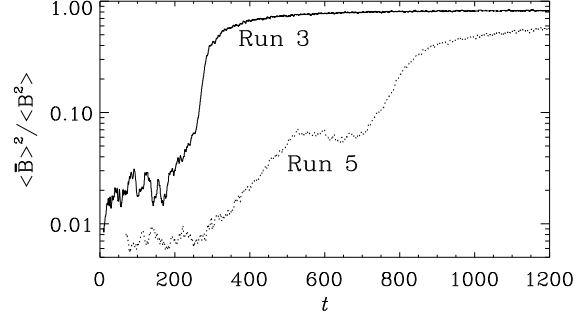


Fig. 7.— Evolution of the filling factor, $\langle \hat{B} \rangle^2 / \langle B^2 \rangle$, for Runs 3 and 5. Note that strong large scale fields are obtained even for large magnetic Reynolds and Prandtl numbers.

3.3. Spectral helicity and energy transfer

The prime reason for the large scale field generation is related to magnetic helicity conservation. Once helicity is injected into the system, it tends to make the magnetic field also helical, as is seen from Fig. 8. For a closed or periodic system however the net magnetic helicity is conserved, except for diffusion at small scales, i.e.

$$\frac{d}{dt} \langle \mathbf{A} \cdot \mathbf{B} \rangle = -2\eta \langle \mathbf{J} \cdot \mathbf{B} \rangle. \quad (11)$$

Thus, if the magnetic field is to become helical, it must at first have equal amounts of positive and negative helicity. This is a feature also seen in hydrodynamical simulations (Biferale & Kerr 1995). At later times, however, magnetic diffusion can destroy magnetic helicity at small scales, leaving magnetic helicity of opposite sign at large scales. This is best described by the evolution equation of the magnetic helicity spectrum which can be derived from the Fourier transformed induction equation (3),

$$\frac{\partial \hat{\mathbf{A}}_{\mathbf{k}}}{\partial t} = \hat{\mathcal{E}}_{\mathbf{k}} - \eta \hat{\mathbf{J}}_{\mathbf{k}}, \quad (12)$$

where hats and subscripts \mathbf{k} indicate three-dimensional Fourier transformation, and $\mathcal{E} = \mathbf{u} \times \mathbf{B}$ is the electromotive force. We write down the corresponding equation for the evolution of $\hat{\mathbf{B}}_{\mathbf{k}} = i\mathbf{k} \times \hat{\mathbf{A}}_{\mathbf{k}}$ and derive from those equations the evolution equation for $\hat{\mathbf{A}}_{\mathbf{k}} \cdot \hat{\mathbf{B}}_{\mathbf{k}}^*$, where asterisks denote complex conjugation. Note that this

is gauge invariant, because adding a gradient to $\hat{\mathbf{A}}_k$ corresponds to adding an $i\mathbf{k} \cdot \hat{\mathbf{B}}_k^*$ term which vanishes, because the magnetic field is solenoidal. We denote the real parts of the shell-integrated spectra of $\hat{\mathbf{A}}_k \cdot \hat{\mathbf{B}}_k^*$ and $\hat{\mathcal{E}}_k \cdot \hat{\mathbf{B}}_k^*$ by $H_M(k, t)$ and $S_M(k, t)$, respectively, and obtain

$$\frac{\partial}{\partial t} H_M(k, t) = 2S_M(k, t) - 2\eta k^2 H_M(k, t). \quad (13)$$

Note that $\int H_M(k, t) dk = \langle \mathbf{A} \cdot \mathbf{B} \rangle$ and, because of helicity conservation, $\int S_M(k, t) dk = 0$, so it makes sense to write Eq. (13) in the form

$$\frac{\partial}{\partial t} H_M(k, t) = -\frac{\partial}{\partial k} G_M(k, t) - 2\eta k^2 H_M(k, t), \quad (14)$$

where we have defined the spectral flux of helicity,

$$G_M(k, t) = \int_k^\infty 2S_M(k', t) dk', \quad (15)$$

which is plotted in Fig. 9 for different times. The magnetic helicity flux, $G_M(k, t)$, is found to be always positive and its peak shifts from small scales ($k \approx 10$) at early times to large scales ($k = 2 - 3$) at later times when the magnetic field becomes dynamically important. Positive magnetic helicity is being produced on the right of the maximum of $G_M(k, t)$ and negative on the left; see Fig. 10.

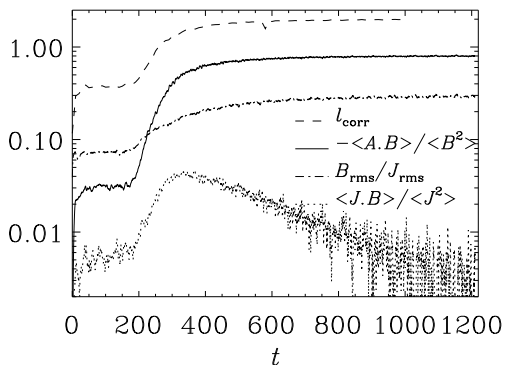


Fig. 8.— Evolution of $-\langle \mathbf{A} \cdot \mathbf{B} \rangle / \langle \mathbf{B}^2 \rangle$, compared with other magnetic length scales. Run 3.

In view of the realizability condition,

$$E_M(k, t) \geq \frac{1}{2} k H_M(k, t) \quad (16)$$

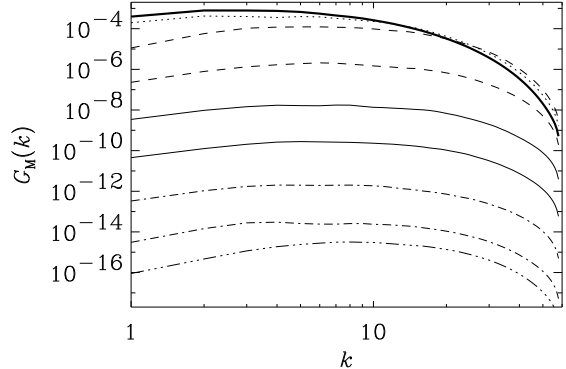


Fig. 9.— Spectra of magnetic helicity flux at $t = 10, 30, 60$ (dot-dashed), 100 and 130 (solid), 160 and 200 (dashed), 300 (dotted), and for the time average between $t = 600$ and 1000 (thick line).

(e.g. Moffatt 1978), the spectral magnetic helicity can be viewed as the *driver* of spectral magnetic energy: while small scale magnetic helicity is being destroyed, an equal amount gets into the large scales, and this must necessarily enhance the magnetic energy so as to satisfy (16). Indeed, in the present simulations the inequality (16) is almost saturated at all scales, except at intermediate scales $2 \leq k \leq 4$; see Fig. 11.

In order to determine the dominant interactions leading to the generation of the large scale field at $k = 1$ we now consider the spectral energy equation,

$$\frac{\partial}{\partial t} E_M(k, t) = 2T_M(k, t) - 2\eta k^2 E_M(k, t), \quad (17)$$

where the transfer function of magnetic energy, $T_M(k, t)$, is the shell-integrated spectrum of the real part of $\hat{\mathcal{E}}_k \cdot \hat{\mathbf{J}}_k^*$. Since $\mathcal{E} = \mathbf{u} \times \mathbf{B}$, this corresponds really to a triple product,

$$\sum_{\mathbf{k}=\mathbf{p}+\mathbf{q}} (\hat{\mathbf{u}}_{\mathbf{p}} \times \hat{\mathbf{B}}_{\mathbf{q}}) \cdot \hat{\mathbf{J}}_{\mathbf{k}}^*, \quad (18)$$

where the skew product can also be written as $-\hat{\mathbf{u}}_{\mathbf{p}} \cdot (\hat{\mathbf{J}}_{\mathbf{k}}^* \times \hat{\mathbf{B}}_{\mathbf{q}})$, emphasizing that this term corresponds to the work done against the Lorentz force. In order to identify the dominant interactions we have calculated, in real space, the spectral transfer

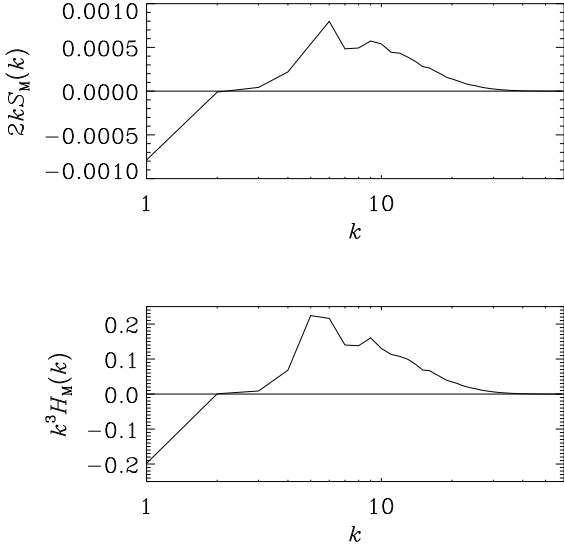


Fig. 10.— Divergence of magnetic helicity flux, $S_M(k)$, scaled by k , so the area under the positive and negative parts of the curve are the same when plotted in a lin-log plot. Because of resistive losses of positive magnetic helicity at small scales, the resulting magnetic helicity, $H_M(k)$, is now dominated by negative helicity at large scales. The lower plot shows $H_M(k)$, scaled by k^3 to show the contributions from small scales. Both spectra are time averages over the interval $600 \leq t \leq 1000$.

matrix

$$T_M(k, p, q, t) = -\langle \mathbf{u}_p \cdot (\mathbf{J}_k \times \mathbf{B}_q) \rangle, \quad (19)$$

where angular brackets denote volume averages and the subscripts k , p , and q denote Fourier filtering around the corresponding wavenumber (by $\pm 1/2$). (In this notation $\langle \mathbf{A}_k \cdot \mathbf{B}_k \rangle$, for example, is exactly the same as the helicity spectrum.)

In Fig. 12 we show $T(k, p) = \sum_q T(k, p, q)$, normalized by $\langle \mathbf{B}^2 \rangle$ for the corresponding times, for $k = 1$ and 2. This function shows that most of the energy of the large scale field at $k = 1$ comes from velocity and magnetic field fluctuations at the forcing scale, $k = 5$. At early times this is also true of the energy of the magnetic field at $k = 2$, but at late times, $t = 1000$, the gain from the forcing scale, $k = 5$, has diminished, and instead there is now a net loss of energy into the next larger scale,

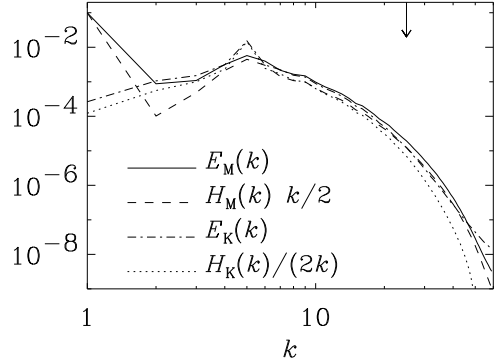


Fig. 11.— Time-averaged spectra of kinetic and magnetic energy, as well as kinetic and magnetic helicity. Note that the magnetic energy exceeds the kinetic energy at $k = 1$, and that the inequality (16) is almost saturated, except near $k = 2$ and 3. The corresponding realizability condition for the kinetic helicity, on the other hand, is not very sharp. The dissipative cutoff wavenumber, $(\omega^2/\nu^2)^{1/4}$, is indicated by an arrow at the top.

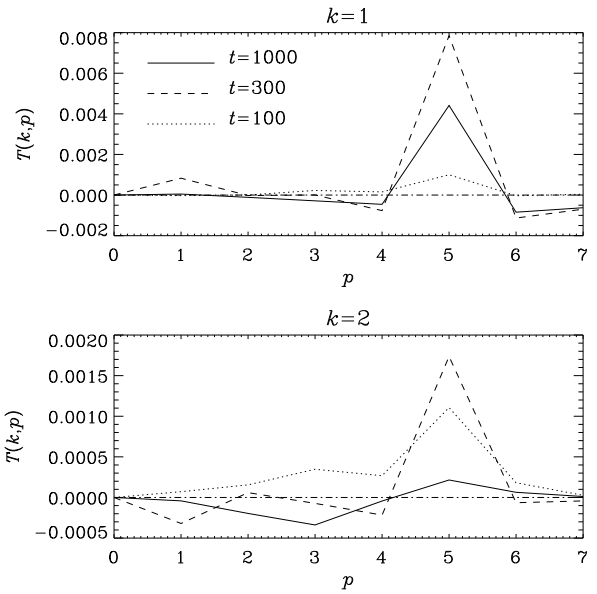


Fig. 12.— Spectral energy transfer function $T(k, p, t)$, normalized by $\langle \mathbf{B}^2 \rangle$ for three different times, for $k = 1$ and 2. Run 3.

$k = 3$, suggestive of a direct cascade operating at

$k = 2$, and similarly at $k = 3$.

The generation of large scale energy at $k = 1$ through *nonlocal* inverse energy transfer is characteristic of the α -effect in mean-field electrodynamics. In the following we shall pursue this analogy further. It should be emphasized, however, that without the simultaneous loss of energy at the next smaller scales (here $k = 2$ and 3) through direct energy transfer the $k = 1$ field would have been totally swamped by smaller scale fields. Thus, nonlinearity is quite crucial for this process to produce well defined large scale fields. Indeed, in the absence of the nonlinear term $\mathbf{J} \times \mathbf{B}$ in Eq. (2) the marked large scale pattern (Fig. 4) disappears in a fraction of a turnover time.

3.4. Mean-field interpretation

In this subsection we adopt the hypothesis that the large scale component of the field at wavenumber $k = 1$ can be described in terms of mean-field theory. The magnetic field at other wavenumbers is ($k \geq 2$) is important for contributing to the α -effect and the turbulent magnetic diffusivity, η_t , but apart from that it is merely an extra source of noise as far as the dynamics of the large scale field is concerned. As we have seen in the previous section, this extra noise is automatically kept to a minimum due to direct cascade effects and transfer to kinetic energy.

According to mean-field theory for non-mirror symmetric isotropic homogeneous turbulence with no mean flow the mean magnetic field is governed by the equation

$$\frac{\partial}{\partial t} \bar{\mathbf{B}} = \alpha \nabla \times \bar{\mathbf{B}} + \eta_T \nabla^2 \bar{\mathbf{B}}, \quad (20)$$

where bars denote the mean fields, α and $\eta_T = \eta_t$ are constants, and η_t is the turbulent magnetic diffusivity. In general, those coefficients are not constant and depend for example on the magnetic field. (In our particular case the local magnetic energy density is however approximately uniform.) Furthermore, since the magnetic field is strong, α and η_t should really be replaced by tensors, but we shall ignore this additional modification except that we shall allow α and η_t to vary slowly in time as the magnetic field approaches saturation. This simplified form of nonlinearity may be justified by noting that the mean magnetic field looks nearly sinusoidal (Fig. 5).

Equation (20) permits steady force-free solutions where the current helicity of the large scale field, $\bar{\mathbf{J}} \cdot \bar{\mathbf{B}}$ is given by $(\eta_T/\alpha) \bar{\mathbf{J}}^2$. Apart from some common phase factor, the mean field depicted in Fig. 5 is given by $\bar{\mathbf{B}}(y) = (\sin y, 0, \cos y)$, so $\bar{\mathbf{J}} = (-\sin y, 0, -\cos y)$, corresponding to negative helicity, and therefore α must be negative. This is in agreement with mean-field theory which predicts that α is a negative multiple of the residual (kinetic minus current) helicity (e.g. Blackman & Chou 1997, Field, Blackman, & Chou 1999), which is positive in our case; see Table 1.

If the wavevector of the large scale field is K_y (as in the case discussed above), Eq. (20) becomes

$$\dot{\bar{\mathbf{B}}}_x = +\alpha \bar{\mathbf{B}}'_z + \eta_T \bar{\mathbf{B}}''_x, \quad (21)$$

$$\dot{\bar{\mathbf{B}}}_z = -\alpha \bar{\mathbf{B}}'_x + \eta_T \bar{\mathbf{B}}''_z, \quad (22)$$

where dots and primes denote differentiation with respect to t and y , respectively. Since $\alpha < 0$, the solution can be written in the form

$$\bar{\mathbf{B}}_x(y, t) = b_x(t) \sin(y + \phi), \quad (23)$$

$$\bar{\mathbf{B}}_z(y, t) = b_z(t) \cos(y + \phi), \quad (24)$$

where $b_x(t)$ and $b_z(t)$ are positive functions of time that satisfy

$$\dot{b}_x = |\alpha| b_z - \eta_T b_x, \quad (25)$$

$$\dot{b}_z = |\alpha| b_x - \eta_T b_z. \quad (26)$$

In a steady state $|\alpha| = \eta_T$, and $b_x = b_z$. In order to find the actual values of $|\alpha|$ and η_T during both the saturated steady state and the growth phase we can do a simple experiment: suppose we put $b_x = 0$ at some moment in time, then Eq. (25) would predict that b_x starts to recover at the rate $|\alpha| b_z$, which allows us to estimate α .

In order to have a somewhat more precise estimate we need the solution to (25) and (26) for the initial condition $b_x(0) = 0$:

$$b_x = e^{(|\alpha| - \eta_T)t} - e^{-(|\alpha| + \eta_T)t}, \quad (27)$$

$$b_z = e^{(|\alpha| - \eta_T)t} + e^{-(|\alpha| + \eta_T)t}, \quad (28)$$

where the amplitude is arbitrary in linear theory. Adding and subtracting (27) and (28) we can solve for $|\alpha| - \eta_T$ and $|\alpha| + \eta_T$, respectively. In terms of $|\alpha|$ and η_T separately, we have

$$|\alpha| = \frac{1}{2} \frac{d}{dt} [+\ln(+b_x + b_z) - \ln(-b_x + b_z)], \quad (29)$$

$$\eta_T = \frac{1}{2} \frac{d}{dt} [-\ln(+b_x + b_z) - \ln(-b_x + b_z)]. \quad (30)$$

In practice we average the results of (29) and (30) over some 5–10 time units. We have applied this method to Runs 1–3 at times between $t = 100$ – 600 and to Run 5 at times between $t = 300$ – 1600 (Fig. 13). During those times the mean field was still evolving (Fig. 6), so at different times the mean magnetic field was different, which allows us to obtain the $\alpha(|\mathbf{B}|)$ dependence. We take into account the fact that during the experiment the actual field is only $1/\sqrt{2}$ of what it was before one of the two components of the mean field has been removed. We have then attempted a fit of the form

$$\alpha = \frac{\alpha_0}{1 + \alpha_B \langle \bar{\mathbf{B}}^2 \rangle / B_{\text{eq}}^2}, \quad (31)$$

where $B_{\text{eq}}^2 = \mu_0 \rho_0 \langle \mathbf{u}^2 \rangle_{\text{sat}}$. The result is shown in Fig. 14 and the coefficients α_0 and α_B are listed in Table 2. One should note, however, that Eq. (31) does not accurately represent the actual data of Run 5. Nevertheless, it is clear that α -quenching is enhanced for large values of R_m , which may be described by a fit of the form

$$\alpha_B \approx (R_m/180)^{1.3}, \quad (32)$$

which is consistent with the result of Vainshtein *et al.* (1993), even though the filling factor is not at all small (Fig. 7), in contrast to their original assumption. The extreme quenching implied by Eq. (32) would suggest that the α -effect cannot be responsible for large scale field generation in the high R_m limit (Vainshtein & Cattaneo 1992). Equation (32) shows that significant quenching only begins when R_m exceeds a few hundred, which may explain why this effect was not seen, for example, in simulations of dynamo action in accretion discs (Brandenburg & Donner 1997), where R_m was 100–200. It should also be noted that both α_0 and α_0/u_{sat} increase with R_m , enhancing thus the dynamo efficiency for up to modestly strong fields.

In Fig. 15 we compare with the result for α obtained by just imposing a uniform magnetic field, $B_0 \mathbf{z}$, and calculating α simply as

$$\alpha^{\text{imp}} = (\langle \mathbf{u} \times \mathbf{B} \rangle)_z / B_0. \quad (33)$$

Each point in Fig. 15 corresponds to a different run with given field strength B_0 , but otherwise

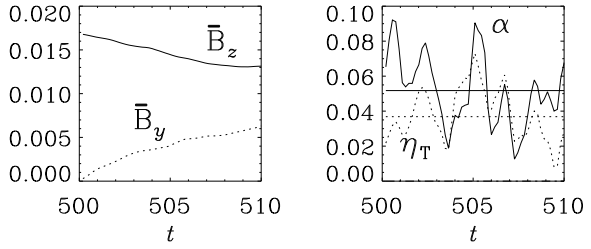


Fig. 13.— Example of the evolution of the mean fields, \bar{B}_y and \bar{B}_z , after subtracting \bar{B}_y from the actual field B_y (left), and the corresponding results for α and η_T (right). The average values are indicated by horizontal lines. Run 5.

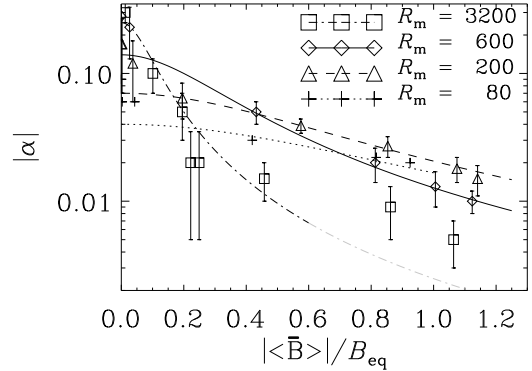


Fig. 14.— Results for α for different values of R_m using Eq. (29). The lines represent the fits described in the text.

the same parameters as in Runs 1–3 and 5. This method was frequently used in the past (e.g. Brandenburg *et al.* 1990, Brandenburg 1993, Tao *et al.* 1993, Cattaneo & Hughes 1996), but it is not *a priori* clear that one measures the same α as with the method explained above. Nevertheless, the two results appear to be qualitatively similar (cf. Figs 14 and 15) although there are some differences in the case where R_m is very large (Table 2).

The only way a strongly R_m -dependent quenching can be compatible with the large scale field generation seen on the present simulations would be if η_T is also strongly quenched. Strong η_T quenching was first suggested by Cattaneo & Vainshtein (1991) using two-dimensional simulations.

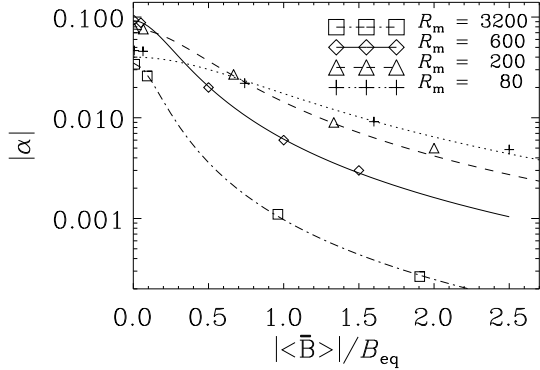


Fig. 15.— Results for α for different values of R_m using an imposed magnetic field. The lines represent the fits described in the text.

Table 2: Coefficients for the α -quenching expressions for 4 runs with different values of R_m .

| | Run 1 | Run 2 | Run 3 | Run 5 |
|---------------------------|-------|-------|-------|-------|
| R_m | 80 | 200 | 600 | 3200 |
| $ \alpha_0 $ | 0.04 | 0.07 | 0.14 | 0.30 |
| α_B | 1.4 | 2.4 | 10 | 100 |
| $ \alpha_0^{\text{imp}} $ | 0.040 | 0.076 | 0.092 | 0.035 |
| α_B^{imp} | 1.3 | 4.3 | 14 | 35 |

However, Gruzinov & Diamond (1995) found that the R_m dependent quenching is not recovered in three dimensions.

In Fig. 16 we compare the results obtained for η_T with the turbulent diffusion coefficient for a passive scalar. The passive scalar diffusion coefficient is obtained by simultaneously solving an additional equation for c ,

$$\frac{D c}{D t} = \frac{1}{\rho} \nabla \cdot \rho D \nabla c, \quad (34)$$

where $D = \eta$ is chosen for Runs 1–3 and $D = 2.5\eta$ for Run 5. The total (turbulent plus microscopic) passive scalar diffusion coefficient is obtained by measuring the rate at which a narrow gaussian distribution of c widens as time goes on. The result is shown in the second panel of Fig. 16. Generally the suppression of η_T by magnetic fields is stronger than the suppression of D_T . (For Run 3 D_T/D ranges between 40 for weak fields and 10 for strong fields.) We note that a dependence of

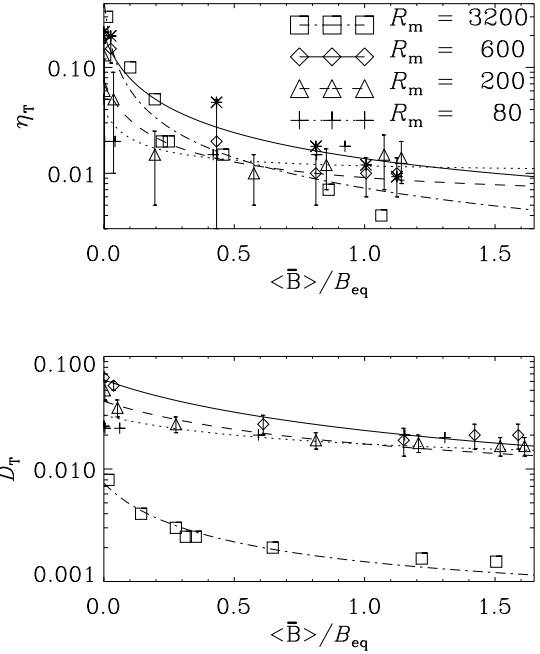


Fig. 16.— Results for η_T and D_T for different values of R_m . The lines represent the fits described in the text. In the plot of η_T the asterisks denote $|\alpha| - \lambda$ for the $R_m = 600$ run, which agrees reasonably well with η_T .

the form

$$D_T = D + D_0 / (1 + D_B \langle |\bar{B}| \rangle / B_{eq}) \quad (35)$$

seems to fit at least the D_T data better than a quadratic dependence. Unlike the results for α , the dependence of D_B on Reynolds number is here less strong. In the fits shown in Fig. 16 a good fit is $D_B = 2$ for all three runs, and $D_0 = 0.02, 0.035$, and 0.06 for Runs 1, 2, and 3, respectively. Run 5 behaves differently, because in this large magnetic Prandtl number run there is basically no inertial range, and so we used $D_0 = 0.007$ and $D_B = 6$.

Using for η_T a similar fit formula as Eq. (35) we have $\eta_B = 16$ for all three runs, and $\eta_0 = 0.03, 0.07$, and 0.2 for Runs 1, 2, and 3, respectively, and $\eta_0 = 0.43$, $\eta_B = 60$ for Run 5. However, for strong magnetic fields, η_T levels off at a value of 0.01 (for Run 3) or 0.005 (for Run 5). Those values are similar to the values of α . Thus, $\alpha \approx \eta_T k_1$, which means that the mean-field dynamo has turned into a marginally critical state,

which is indeed to be expected. As a consistency check for the directly obtained values of η_T we use the time dependent growthrate $\lambda(t)$ and show $|\alpha| - \lambda$ (asterisks in Fig. 16) for the $R_m = 600$ run. They agree reasonably well with η_T (except near $\langle |\mathbf{B}| \rangle = 0.4B_{\text{eq}}$), suggesting that (25) and (26) are approximately satisfied with the coefficients obtained above. However, the combination of fits for α and η_T does not allow us to obtain reliable estimates for the final equilibrium field strength, which turns out to be a weakly increasing function of R_m ; see Sect 3.6.

3.5. Large scale separation

In some earlier exploratory models we forced the flow at $k = 10$, which gave somewhat more room for the inverse cascade to develop, but less room for the direct cascade toward smaller wavenumbers. The latter means that the Reynolds number with respect to the forcing scale is smaller and the turbulent mixing properties, as quantified by the ratio D_t/D , are poorer. Strong turbulent mixing was important in order to address the issue of Reynolds number dependent suppression of transport coefficients. In this subsection we shall accept poor mixing in favor of larger scale separation and hence a significantly larger subrange in which the inverse cascade can develop. Thus, we now force the flow at $k = 30$ (Run 6).

After saturation is reached, which happens first at some intermediate scale, there is a wave of spectral energy propagating toward smaller k . This is similar to the results of closure models of Pouquet *et al.* (1976). However, unlike those models there does not seem to develop a k^{-1} magnetic energy spectrum. Instead, there is only an *envelope* of the helicity wave that follows approximately a k^{-1} powerlaw (Fig. 17). As before, there is a strong built-up of magnetic energy at the largest scale, $k = 1$, combined with a subsequent suppression of energy at intermediate scales ($2 \leq k \leq 20$). The ratio of the peak value at $k_1 = 1$ to the value of the secondary peak at the forcing scale $k_f = 30$ scales like $(k_1/k_f)^{-1}$ (Fig. 17). This is also the case in runs with $k_f = 5$ (Fig. 11).

As a function of time, the spectral magnetic energy grows at the same rate at all values of k until saturation is reached. During early times the magnetic spectra peak at $k_{\text{max}} \approx 7$, which is also the wavenumber that reaches equipartition first,

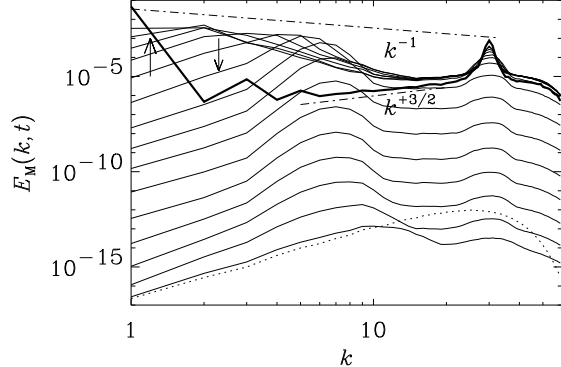


Fig. 17.— Magnetic energy spectra for Run 6 with forcing at $k = 30$. For orientation k^{-1} and $k^{+3/2}$ slopes are given as dash-dotted lines. The times range from 0 (dotted line) to 10, 30, ..., 290 (solid lines). The thick solid line gives the final state at $t = 1000$. Note that at early times the spectra peaks at $k_{\text{max}} \approx 7$.

but then the field at this wavenumber decays to a somewhat smaller value while the contributions from the next smaller k grow and subsequently decay; see Fig. 18. Finally, when the energy at $k = 1$ reaches equipartition the energy of all larger k s becomes suppressed.

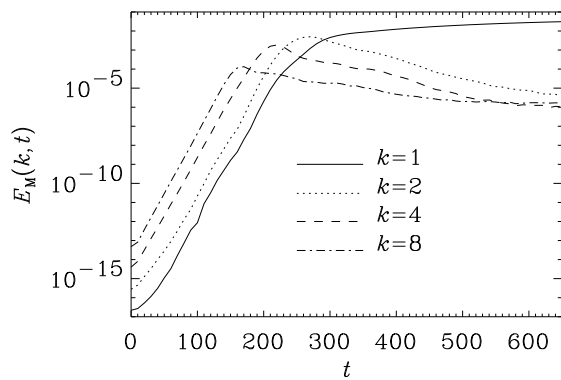


Fig. 18.— Evolution of spectral magnetic energy for selected wavenumber in a simulation with forcing at $k = 30$.

Although a comparison with mean-field theory may be inappropriate, it is interesting to note that

the existence of a k_{\max} is predicted from the theory of α^2 dynamos in infinite media (Moffatt 1978). The dispersion relation is

$$\lambda = |\alpha|k - \eta_T k^2, \quad (36)$$

where λ is the growth rate. Maximum growth occurs at wavenumber

$$k_{\max} = \frac{1}{2}|\alpha|/\eta_T, \quad (37)$$

and there the maximum growth rate is

$$\lambda_{\max} = \frac{1}{2}|\alpha|k_{\max}. \quad (38)$$

Since k_{\max} and λ_{\max} can be measured, we can determine

$$|\alpha| = 2\lambda_{\max}/k_{\max}, \quad \eta_T = \lambda_{\max}/k_{\max}^2 \quad (39)$$

during the growth phase of the dynamo. With $k_{\max} = 7$ (Fig. 18) and $\lambda_{\max} = 0.14$ (Fig. 17) we have $|\alpha| = 0.04$ and $\eta_T = 0.003$. In this case, the forcing occurs essentially in the dissipation range, so the turbulence has therefore relatively poor mixing properties. Since in this run the microscopic value of η was 0.002, the turbulent contribution is only half as big. The value of α is about 4 times smaller than that of Run 3 during the kinematic regime, which seems reasonable.

In the nonlinear regime there are marked differences between mean-field theory and simulations. Using a nonlinear mean-field model of the inverse cascade with α -effect, Galanti, Sulem, & Gilbert (1991) found significant power at $k \geq 2$, which is in contrast to the behavior seen in Fig. 17. Consequently, the mean fields of Galanti, Gilbert, & Sulem (1990) look much less sinusoidal than in the simulations (Fig. 5). If one wanted to model this within the framework of an α -effect one would need to invoke a scale-dependent α integral kernel, where the dominant contributions to α come only from the largest scale of the system (Brandenburg & Sokoloff 2000).

3.6. Reynolds number dependence and magnetic helicity

We now discuss to which extent our results are affected by the limited resolution and finite magnetic Reynolds number. In Fig. 19 we show energy spectra of the magnetic field for three values of R_m . The three curves differ by a certain

factor, but are otherwise essentially the same at small wavenumbers. The main difference is, as expected, at the smaller scales: the spectra for large R_m begin to show signs of an inertial range for values of k larger than the forcing wavenumber.

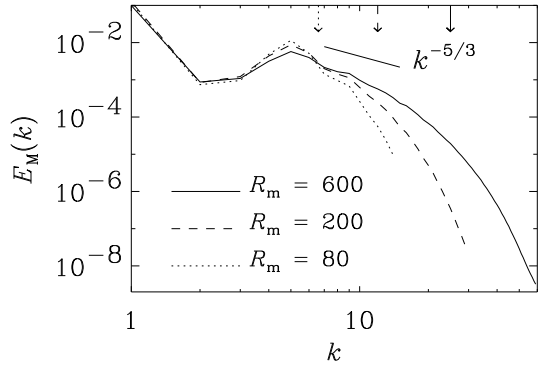


Fig. 19.— Comparison of time averaged magnetic energy spectra for Runs 1–3 ($t = 600 – 1000$). To compensate for different field strengths and to make the spectra overlap at large scales, two of the three spectra have been multiplied by a scaling factor ($\times 2$ for Run 2 and $\times 5$ for Run 1). There are clear signs of the gradual development of an inertial subrange for wavenumbers larger than the forcing scale. The $k^{-5/3}$ slope is shown for orientation. The dissipative magnetic cutoff wavenumbers, $\langle \mathbf{J}^2/\eta^2 \rangle^{1/4}$, are indicated by arrows at the top.

Although the magnetic energy spectra of the statistically steady state seem to show convergence to a spectrum roughly compatible with $k^{-5/3}$, there are some serious concerns about the *timescale* on which such a steady state is achieved. As was first pointed out by Berger (1984), in a closed box (periodic or perfectly conducting) there is an upper bound on the rate of change of the magnetic helicity. This is relevant, because the fields that are generated in the simulations have strong magnetic helicity: $\langle \mathbf{A} \cdot \mathbf{B} \rangle / \langle \mathbf{B}^2 \rangle \approx -0.8/k_1$ (Fig. 8). Most of the magnetic helicity is in the large scales (Fig. 11). In order to build up the helicity at large scales we have to destroy magnetic helicity at small scales (Fig. 9).

Open boundary conditions would help to get rid of magnetic helicity (cf. Blackman & Field 2000),

which may well be an important factor in more realistic simulations (e.g. Glatzmaier & Roberts 1995, Brandenburg *et al.* 1995). However, the present simulations are for closed boxes and yet they do show strong fields, so we need to understand whether and how they have been affected by this constraint.

The rate at which magnetic helicity can change, see Eq. (11), is constrained by the Schwartz inequality,

$$\left| \frac{d}{dt} \langle \mathbf{A} \cdot \mathbf{B} \rangle \right| = 2\eta |\langle \mathbf{J} \cdot \mathbf{B} \rangle| \leq 2\eta J_{\text{rms}} B_{\text{rms}} \quad (40)$$

(Berger 1984, Moffatt & Proctor 1985). In forced systems it is common (albeit not necessary) that the energy (B_{rms}^2) and dissipation rate (ηJ_{rms}^2) are independent of the Reynolds number. However, this would imply that the rate of change of $\langle \mathbf{A} \cdot \mathbf{B} \rangle$ is limited resistively by a term proportional to $\eta^{1/2}$. In our simulations, $\langle \mathbf{J} \cdot \mathbf{B} \rangle / (J_{\text{rms}} B_{\text{rms}})$ has a maximum of ~ 0.25 (see Table 1), so the effects of this limit are therefore not directly seen in the simulations.

There is a related and even more important consequence of Eq. (11). In a steady state, $\langle \mathbf{A} \cdot \mathbf{B} \rangle$, which is gauge invariant and therefore physically meaningful, must be constant, and hence $\langle \mathbf{J} \cdot \mathbf{B} \rangle \rightarrow 0$. Thus, although we are going to generate a strong large scale field with significant current helicity in the large scales, the net current helicity must actually vanish. This can only happen if there is an equal amount of small scale current helicity of opposite sign, i.e.

$$\langle \mathbf{j} \cdot \mathbf{b} \rangle = -\langle \overline{\mathbf{J}} \cdot \overline{\mathbf{B}} \rangle \quad (\text{in the steady state}), \quad (41)$$

where angular brackets denote volume averages, bars denote the large scales at $k = 1$, and lower characters refer to contributions from all higher wavenumbers. To summarize this, in the steady state and with closed boundary conditions we must have finite net magnetic helicity, but zero net current helicity. Furthermore, at *small* scales there must be a certain amount of current helicity, but relatively little magnetic helicity. This is possible because the current helicity spectrum, which is $k^2 H_M(k)$ in the isotropic case, peaks at large wavenumbers.

In the following we estimate the evolution of the energy of the large scale field, $\overline{\mathbf{B}}^2$, using the fact

that in the present simulations the magnetic field has a large filling factor (Fig. 7) and strong magnetic helicity. This would be too ideal an assumption for astrophysical settings, but it is adequate for describing our present simulations. Thus, we may set

$$k_1 \langle \mathbf{A} \cdot \mathbf{B} \rangle \approx \langle \overline{\mathbf{J}} \cdot \overline{\mathbf{B}} \rangle / k_1 \approx -\langle \overline{\mathbf{B}}^2 \rangle. \quad (42)$$

For clarity we retain here the k_1 factors, even though they are one. Using Eq. (11) this yields

$$\frac{d}{dt} \langle \overline{\mathbf{B}}^2 \rangle \approx -2\eta k_1^2 \langle \overline{\mathbf{B}}^2 \rangle + 2\eta k_1 |\langle \mathbf{j} \cdot \mathbf{b} \rangle|, \quad (43)$$

which has the solution

$$\overline{\mathbf{B}}^2 \approx 2\eta k_1 e^{-2\eta k_1^2 t} \int_{t_{\text{sat}}}^t e^{2\eta k_1^2 t'} |\langle \mathbf{j} \cdot \mathbf{b} \rangle| dt', \quad (44)$$

which is expected to apply after the time of saturation, $t = t_{\text{sat}}$, when $\langle \mathbf{j} \cdot \mathbf{b} \rangle$ is approximately constant, so

$$\overline{\mathbf{B}}^2 = \epsilon_0 B_{\text{eq}}^2 \left[1 - e^{-2\eta k_1^2 (t - t_{\text{sat}})} \right] \quad (45)$$

where, again, $B_{\text{eq}}^2 = \mu_0 \rho_0 \langle \mathbf{u}^2 \rangle_{\text{sat}}$, but we have allowed for a factor ϵ_0 . For Runs 1–3 and 5, good agreement with the simulations is obtained when $\epsilon_0 = 1.85, 2.84, 3.58$, and 7.0 , and $t_{\text{sat}} = 600, 330, 280$, and 600 , respectively; see Fig. 20. In the large magnetic Reynolds number case t_{sat} is particularly long, but if expressed in terms of turnover times, $t_{\text{sat}} u_{\text{sat}} / L$ varies much less ($12, 8, 8, 10$, for Runs 1–3 and 5, respectively).

One may expect that ϵ_0 scales like $R_m^{1/2}$, because $|\langle \mathbf{j} \cdot \mathbf{b} \rangle| / \overline{\mathbf{B}}^2 \sim J_{\text{rms}} / B_{\text{rms}}$ is the square root of the inverse magnetic Taylor microscale, which should vary like $R_m^{1/2}$. However, our data are more consistent with a scaling of the form

$$\epsilon_0 \approx (R_m / 14)^{+0.35}. \quad (46)$$

The discrepancy with the anticipated $R_m^{1/2}$ scaling could be related to the lack of a fully developed inertial range. Nevertheless, although the maximum strength of the mean field increases with R_m , the time it takes to approach this maximum increases proportional to R_m . However, as discussed above, the time after which the large scale field *begins* to develop is essentially t_{sat} , which is much shorter and probably independent of R_m .

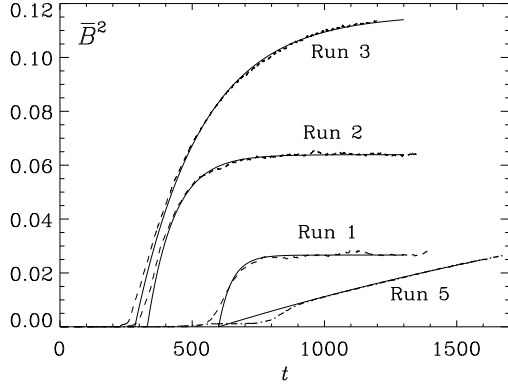


Fig. 20.— Evolution of \bar{B}^2 for Runs 1–3 and Run 5, compared with the approximation (45).

The resistively limited growth of \bar{B} has immediate consequences for α . The evolution equation for $\langle \bar{A} \cdot \bar{B} \rangle$ can be derived from Eq. (20),

$$\frac{d}{dt} \langle \bar{A} \cdot \bar{B} \rangle = 2\alpha \langle \bar{B}^2 \rangle - 2\eta_T \langle \bar{J} \cdot \bar{B} \rangle. \quad (47)$$

In the strongly helical case considered here the magnetic helicity of the large scale field, $\langle \bar{A} \cdot \bar{B} \rangle$, is very nearly equal to $\langle A \cdot B \rangle$, so the right hand sides of (11) and (47) must be approximately equal, which leads to

$$|\alpha| - \eta_T k_1 \approx \eta |\langle \bar{J} \cdot \bar{B} \rangle| / \langle \bar{B}^2 \rangle. \quad (48)$$

In order to check this relation we plot the two sides of (48) versus time (Fig. 21), where $\eta_T = \eta + \eta_t$ and $|\alpha| - \eta_t k_1$ has been obtained directly from $\mathcal{E} = \mathbf{u} \times \mathbf{B}$ assuming $\bar{\mathcal{E}} = \alpha \bar{B} - \eta_t \bar{J}$ which, for fully helical mean fields, leads to

$$|\alpha| - \eta_t k_1 = |\langle \bar{\mathcal{E}} \cdot \bar{B} \rangle| / \langle \bar{B}^2 \rangle. \quad (49)$$

Note that in our case $\alpha < 0$, so $\langle \bar{\mathcal{E}} \cdot \bar{B} \rangle < 0$. The constraint (48) on α reflects the fact that the growth of the large scale field is limited by the microscopic resistivity, as seen from Eq. (45). Note, however, that this statement only applies to the present case of strong helicity and closed or periodic boxes.

We note that there have been previous attempts to incorporate the conservation of helicity into the expression for α , which led to a dynamical dependence of α on time and field strength (Kleeorin,

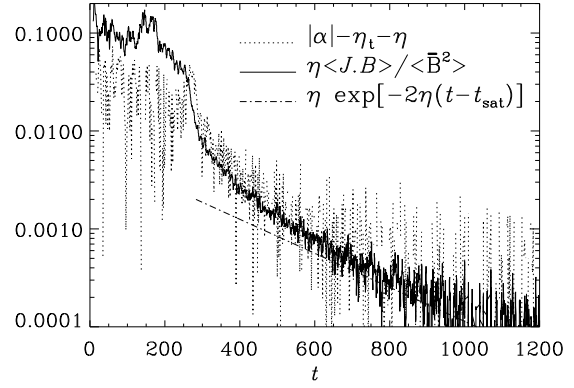


Fig. 21.— Comparison of $|\alpha| - \eta_T k_1$ with $\eta \langle \bar{J} \cdot \bar{B} \rangle / \langle \bar{B}^2 \rangle$ and $\eta \exp[-2\eta k_1^2(t - t_{\text{sat}})]$. Note that $|\alpha| - \eta_T k_1$ follows very closely the resistively dominated limit. Notice also the relatively large noise level in $|\alpha| - \eta_T$. Run 3.

Rogachevskii, & Ruzmaikin 1995, Kleeorin *et al.* 2000). Note, however, that their approach has been criticized (Blackman & Field 1999).

3.7. Large magnetic Prandtl numbers

The magnetic helicity constraint becomes more important as the magnetic Reynolds number is increased. So far we have mainly considered the case where $\nu/\eta = 1$. In the sun and many other astrophysical bodies, $\nu/\eta \ll 1$, but in the galaxy $\nu/\eta \gg 1$ (e.g. Kulsrud & Andersen 1992). This may lead to a magnetic energy spectrum peaking at small scales (Kulsrud & Andersen 1992). However, although viscous damping will limit the field at small scales (Chandran 1998, Kinney *et al.* 1998), there is some evidence that the inverse cascade may no longer operate (Cowley 2000, Maron 2000). Those results have been obtained in the absence of net helicity. It will therefore be interesting to see whether in the presence of net helicity an inverse cascade is still possible when $\nu/\eta \gg 1$.

In a preliminary attempt to clarify this question we have carried out simulations for $\nu/\eta = 20$ (mainly by lowering the viscosity to $\nu = 0.02$; Run 4) and $\nu/\eta = 100$ (where also the magnetic diffusivity was lowered to $\eta = 2 \times 10^{-4}$; Run 5). The viscous cutoff wavenumber is then around 5, i.e. at the forcing scale, and the magnetic cutoff

wavenumbers are 25 and 72, respectively.

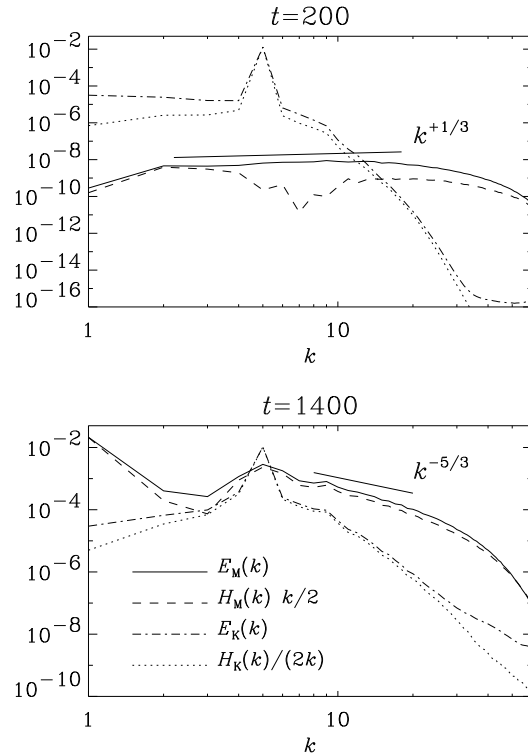


Fig. 22.— Spectra of magnetic and kinetic energy and helicity for a large magnetic Prandtl number at early and late times. $\nu = 0.02$, $\eta = 2 \times 10^{-4}$.

As seen from Fig. 22 the magnetic energy spectrum does indeed peak at large wavenumbers initially, although the magnetic energy spectrum does not scale like $k^{3/2}$ (Kulsrud & Andersen 1992). Instead, the spectrum is close to $k^{1/3}$, which was also found during the kinematic stage of convective dynamos (Brandenburg *et al.* 1996). The magnetic energy exceeds the kinetic energy at large wavenumbers, although at later times the kinetic energy is increased somewhat by magnetic forces. However, especially at later times the magnetic energy is no longer dominated by small scales and the spectrum falls off more like $k^{-5/3}$. The convergence to this powerlaw is evident when comparing Runs 3, 4, and 5 (Fig. 23). Most importantly, there are now clear signs of an inverse cascade; see Fig. 24.

In these runs with large magnetic Prandtl number the current density shows strong filamentary

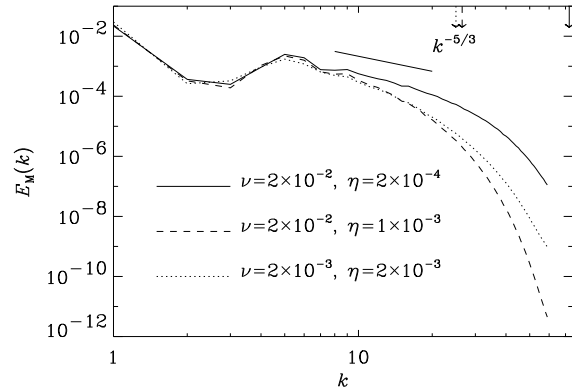


Fig. 23.— Comparison of the magnetic energy spectra for Runs 3, 4 and 5. The magnetic cutoff wavenumbers are 25, 26, and 72, as indicated by arrows at the top.

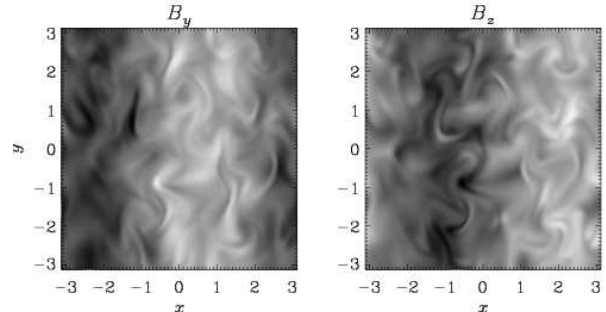


Fig. 24.— Images of the B_y and B_z components of the magnetic field in an arbitrarily chosen xy plane. Run 5, $t = 1600$.

structures that tend to be aligned with the local magnetic field direction, as seen in Fig. 25. The resulting anisotropy affects in particular the small scales (Goldreich & Sridhar 1997, Cowley 2000). Note that this type of anisotropy cannot be captured by closure models (e.g. Pouquet *et al.* 1976).

The main shortcoming of the present large Prandtl number calculations is that the viscous dissipation cutoff wavenumber is so small that it lies in the range of the forcing scale, so no inertial range in the kinetic energy is possible. At the same time, of course, the range of scales available to the magnetic field is still not large enough to establish a $k^{3/2}$ scaling at early times.

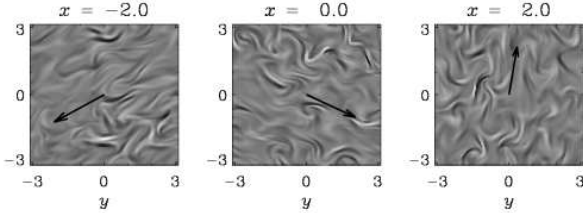


Fig. 25.— Images of the current density, J_x , in the plane of the large scale magnetic field. The field direction is shown as a vector. Run 5, $t = 1600$.

4. Conclusions

The main conclusion to be drawn from this work is that in the presence of net magnetic helicity there is a gradual built-up of a nearly force-free magnetic field at the largest possible scale of the system. In our periodic calculations this corresponds to a sinusoidal one-dimensional Beltrami field, e.g. $\bar{\mathbf{B}} \sim (\cos z, \sin z, 0)$, which is of course locally strongly distorted by the turbulence. Nevertheless, the presence of the large scale field is clearly seen without averaging (Fig. 4). We emphasize that this result is numerically robust: the relative dominance of magnetic energy at the smallest wavenumber is independent of resolution (Fig. 19) and independent of the degree of scale separation (Fig. 17). So, the effect is seen equally well at resolutions ranging from 30^3 to 120^3 mesh-points, and at forcing wavenumbers ranging from 5 to 30. We also note that the results are not very sensitive to the choice of the forcing function: a forcing function that is nearly delta-correlated in space, but still strongly helical, yields very similar results. In the absence of net helicity, however, the large scale field disappears.

An important property of the turbulence is that once the large scale field is established, it can suppress magnetic energy on scales smaller than the largest one. This leads to something like a ‘self-cleaning’ processes. This is also seen in histograms of the magnetic field which are, for the present simulations, more nearly gaussian (with one hump perpendicular to the field, and two in the direction of the field). This is very different from simulations of small scale dynamo action where the histograms of the field components shows stretched exponentials (Brandenburg *et al.* 1996), which can also be seen in the present simulations, but only

at early times.

Our simulations show that most of the energy input to the large scale field comes from small scales around the forcing scale. This is indeed suggestive of an α -effect that could be responsible for the field generation, rather than a local inverse cascade, which transports energy from $k = 2$ to $k = 1$, for example. Although a local inverse cascade does occur at early times, i.e. before the magnetic field is fully established, once the field is strong the magnetic energy in $k = 2$ is actually cascaded to $k = 3$ and/or transferred to kinetic energy, both of which are probably important for the ‘self-cleaning’ processes. A sketch of the anticipated energy transfer properties is given in Fig. 26.

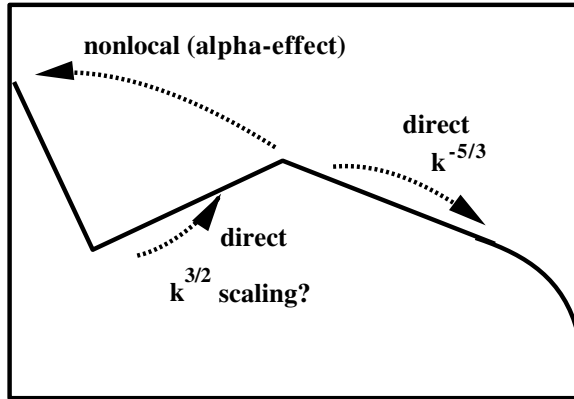


Fig. 26.— Sketch illustrating direct and inverse cascade processes in helical MHD turbulence.

We emphasize that the present simulations must not be regarded as local, because the field structure depends crucially on the size of the box. Instead, they should be viewed as global within the geometry considered. With other boundary conditions or in different geometries the shape of the large scale field will be different. In the case of a sphere, for example, no perfectly force-free field is possible, but the field may be nearly force-free. An example may be the field obtained in hydromagnetic calculations with α -effect (Proctor 1977), where field saturation occurs through the Lorentz force of the large scale field. In those calculations the magnetic saturation field strength is relatively large, which reflects the fact that the field is indeed nearly force-free.

Any reference to an α -effect may be inappropriate here, but at the very least the $\alpha - \Omega$ dy-

namo equations may be regarded as an algorithm for obtaining nearly force-free fields subject to certain constraints. It is perhaps because of this that mean-field theory has been in some ways rather successful. Indeed, there are turbulence calculations relevant to accretion discs where large scale magnetic fields are generated whose properties (field geometry, oscillatory or steady behavior) follow in some detail what is predicted from mean-field theory (Brandenburg 1998). Those tests are however limited in that they do not address questions regarding the functional form of the mean-field equations nor, for example, the possibility of scale dependence of the transport coefficients.

Our simulations show that the mean-field description is not able to reproduce correctly certain aspects of the growth phase of the dynamo. Indeed, at early times when the field is still weak, all scales grow rapidly and the overall field pattern is dominated by smaller scales. At this point the large scale field at $k = 1$ is still just part of the overall spectrum and cannot be treated separately. It is only at later times after the initial saturation of the dynamo that the large scale field at $k = 1$ begins to grow to values large enough so that a clear field pattern becomes noticeable even without averaging. The possible failure of mean-field theory to describe the *growth* of the large scale field may be important when trying to explain the galactic magnetic field, which would grow too slowly according to conventional mean-field theory (e.g. Beck *et al.* 1996). A two-step process (Beck *et al.* 1994) whereby a strong small scale field is generated first, and later modified by large scale dynamo processes, would appear more plausible.

Note that we have not used any subgrid scale modeling or any type of hyperviscosity, which would allow for longer inertial subranges. This seems justified given the rather subtle effects of resistivity on the timescales on which large scale magnetic fields can grow. In the light of Berger's helicity constraint, for example, a careful investigation of the effects of hyperviscosity would be desirable. Our simulations are compatible with the idea that the increase of the large scale field past equipartition happens on a slow resistive timescale. This has become particularly clear in Run 5, where the final selection of the large scale field structure occurred rather late (after

$t \approx 1200$, corresponding to about 20 turnover times; Fig. 6). By contrast, in Run 3, where the magnetic Reynolds number was about 6 times smaller, the large scale field was fully developed by the time $t \approx 400$, corresponding to about 10 turnover times. Those results would suggest that the large scale field is fully developed after about $0.3 R_m^{1/2}$ turnover times. Applied to the sun, this time would correspond to about 300–1000 years, clearly longer than the solar cycle period. However, firstly the sun does have open boundaries and may get rid of small scale helicity rather rapidly (Berger & Ruzmaikin 2000). Secondly, the magnetic helicity does not change sign from one cycle to the next, and it is not clear how that affects our considerations.

Important aspects of future work in this direction include a study of the effects of open boundary conditions to see whether this relaxes the constraint on the growth of the large scale field. Another possibility is to take a domain with spatially variable helicity simulating the effects of an equator through which there could be a continuous helicity flux. Also, it would be important to study the effects of resistive scaling in simulations where the mean field is cyclic, which could be the case in the presence of shear. Finally, of course, real systems are far from having 100% helicity, so it would be important to study simulations that are more realistic in that respect.

I thank the participants of the Astrophysical Turbulence Program at the Institute for Theoretical Physics at the University of California, Santa Barbara, for many valuable discussions. This work was supported by the National Science Foundation through the grant PHY94-07194. Use of the PPARC supported supercomputers in St Andrews and Leicester is acknowledged.

REFERENCES

Balsara, D., & Pouquet, A. 1999, Phys. Plasmas 6, 89

Beck, R., Brandenburg, A., Moss, D., Shukurov, A., & Sokoloff, D. 1996, Ann. Rev. Astron. Astrophys. 34, 155

Beck, R., Poezd, A. D., Shukurov, A., Sokoloff, D. D. 1994, A&A 289, 94

Berger, M. A. 1984, *Geophys. Astrophys. Fluid Dyn.* 30, 79

Berger, M. A., & Ruzmaikin, A. 2000, *JGR* (to appear)

Biferale, L., & Kerr, R. M. 1995, *Phys. Rev. E* 52, 6113

Blackman, E. G. & Chou, T. 1997, *ApJ* (Letters) 489, L95

Blackman, E. G., & Field, G. F. 1999, *ApJ* 521, 597

Blackman, E. G., & Field, G. F. 2000, *ApJ* 534, 984

Brandenburg, A. 1998, in *Theory of Black Hole Accretion Discs*, ed. M. A. Abramowicz, G. Björnsson & J. E. Pringle (Cambridge University Press), p.61

Brandenburg, A. 1993, in *The Cosmic Dynamo*, ed. F. Krause, K.-H. Rädler, & G. Rüdiger (Kluwer Acad. Publ., Dordrecht), p.111

Brandenburg, A., & Donner, K. J. 1997, *MNRAS* 288, L29

Brandenburg, A., & Sokoloff, D. 2000, *GAFD* (submitted)

Brandenburg, A., Nordlund, Å., Pulkkinen, P., Stein, R.F., & Tuominen, I. 1990, *A&A* 232, 277

Brandenburg, A., Nordlund, Å., Stein, R. F., & Torkelsson, U. 1995, *ApJ* 446, 741

Brandenburg, A., Jennings, R. L., Nordlund, Å., Rieutord, M., Stein, R. F., & Tuominen, I. 1996, *J. Fluid Mech.* 306, 325

Cattaneo, F., & Hughes, D. W. 1996, *Phys. Rev. E* 54, R4532

Cattaneo, F., & Vainshtein, S. I. 1991, *ApJ* (Letters) 376, L21

Cowley, S. C. 2000 (presentation at the ITP, <http://online.itp.ucsb.edu/online/astrotc00/cowley/>)

Chandran, B. D. G. 1998, *ApJ* 492, 179

Field, G. B., Blackman, E. G., & Chou, H. 1999, *ApJ* 513, 638

Frisch, U., Pouquet, A., Léorat, J., & Mazure, A. 1975, *J. Fluid Mech.* 68, 769

Galanti, B., Gilbert, A. D., & Sulem, P.-L. 1990, in *Topological Fluid Mechanics*, ed. H. K. Moffatt & A. Tsinober (Cambridge University Press, Cambridge), p.138

Galanti, B., Sulem, P.-L. & Gilbert, A. D. 1991, *Physica D* 47, 416

Glatzmaier, G. A., & Roberts, P. H. 1995, *Nat* 377, 203

Goldreich, P., & Sridhar, S. 1997, *ApJ* 485, 680

Gruzinov, A. V., & Diamond, P. H. 1994, *Phys. Plasmas* 2, 1941

Kazantsev, A. P. 1968, *Sov. Phys. JETP* 26, 1031

Kinney, R. M., Chandran, B. D. G., Cowley, S. C., & McWilliams, J. C. 1998 *AAS* 192, 66.18

Kleeorin, N. I., Rogachevskii, I., & Ruzmaikin, A. 1995, *A&A* 297, 159

Kleeorin, N. I., Moss, D., Rogachevskii, I., & Sokoloff, D. 2000 *A&A* (submitted)

Krause, F., & Rädler, K.-H. 1980, *Mean-Field Magnetohydrodynamics and Dynamo Theory* (Akademie-Verlag, Berlin; also Pergamon Press, Oxford)

Kulsrud, R. M., & Anderson, S. W. 1992, *ApJ* 396, 606

Maron, J. L. 2000 PhD thesis (Caltech)

Meneguzzi, M., Frisch, U., & Pouquet, A. 1981, *Phys. Rev. Lett.* 47, 1060

Moffatt, H. K. 1978, *Magnetic Field Generation in Electrically Conducting Fluids* (Cambridge University Press, Cambridge)

Moffatt, H. K., & Proctor, M. R. E. 1985, *J. Fluid Mech.* 154, 493

Parker, E. N. 1979, *Cosmical Magnetic Fields* (Clarendon Press, Oxford)

Pouquet, A., Frisch, U., & Léorat, J. 1976, *J. Fluid Mech.* 77, 321

Proctor, M. R. E. 1977, *J. Fluid Mech.* 80, 769

Tao, L., Cattaneo, F., & Vainshtein, S. I. 1993, in *Solar and Planetary Dynamos*, ed. M. R. E. Proctor, P. C. Matthews, & A. M. Rucklidge (Cambridge University Press), p.303

Vainshtein, S. I., & Cattaneo, F. 1992, *ApJ* 393, 165

Vainshtein, S. I., Tao, L., Cattaneo, F., & Rosner, R. 1993, in *Solar and Planetary Dynamos*, ed. M. R. E. Proctor, P. C. Matthews, & A. M. Rucklidge (Cambridge University Press), p.311

Ziegler, U., & Rüdiger, G. 2000, *A&A* 356, 1141